Electronic Supplementary Information

Inhibiting Li$^+$ Migration by Thenoyltrifluoroacetone toward Efficient and Stable Perovskite Solar Cells

Yuting Ma,[a] Gaoyi Han,*[a] Meiling Yang,[a] Mengna Guo,[a] Yaoming Xiao,*[b] Yao Guo,*[c] Wenjing Hou*[a]

[a] *Institute of Molecular Science, Key Laboratory of Chemical Biology and Molecular Engineering of Education Ministry, Key Laboratory of Materials for Energy Conversion and Storage of Shanxi Province, State Key Laboratory of Quantum Optics and Quantum Optics Devices, Shanxi University, Taiyuan 030006, P. R. China.*

[b] *College of Chemical Engineering and Materials Science, Quanzhou Normal University, Quanzhou 362000, P. R. China.*

[c] *School of Materials Science and Engineering, Henan Joint International Research Laboratory of Nanocomposite Sensing Materials, Anyang Institute of Technology, Anyang 455000, P. R. China.*

[*] Corresponding authors.

Email: wjhou2016@sohu.com (Wenjing Hou); ymxiao@qztc.edu.cn (Yaoming Xiao); guoyao@ayit.edu.cn (Yao Guo); han_gaoyis@sxu.edu.cn (Gaoyi Han)

1.Experimental section

1.1 Materials. The laser etched indium-doped tin oxide (ITO) glass substrate was purchased from Kunshan Songlight New Energy Technology Co. Ltd. The 4-tert-butylpyridine and SnO$_2$ colloidal dispersion (15 wt.% in H$_2$O) are both from AlfaAesar.2,2',7,7'-tetrakis[N,N-di-(4-methoxyphenyl)amino]-9,9'-

spirobifluorene(Spiro-OMeTAD), poly[bis(4-phenyl)(2,4,6-trimethylphenyl)amine] (PTAA), Cesium iodide (CsI), Lead iodide (PbI$_2$) and CH$_3$NH$_3$Cl (MACl)) were from Xi'an Polymer Light Technology Corp. Ltd. CH$_3$NH$_3$Br (MABr), HC(NH$_2$)$_2$I (FAI) and CH$_3$NH$_3$I (MAI) were from Greatcell Solar Materials Pty. Ltd. Acetonitrile and Thenoyltrifluoroacetone(TTA) were from Aladdin company. Chlorobenzene (CB), Isopropanol (IPA), Anhydrous dimethyl sulfoxide (DMSO), CH$_5$N$_2$Cl (FACl), bis(trifluoromethane sulfuonimide lithium salt (LiTFSI) and N,N-dimethylformamide (DMF) were brought from Sigma. Aldrich, Corp. Ltd.

1.2 Device fabrication. Perovskite solar cell were prepared with planar structure of ITO/SnO$_2$/perovskite/TTA/Spiro-OMeTAD/Ag. After being ultrasonically cleaned with detergent, distilled water and ethanol, the etched ITO glass substrates were treated by UV-ozone for device fabrication. First, the SnO$_2$ film was prepared by spin-coating the diluted SnO$_2$ colloidal solution ($V_{colloidal}$:V_{water}=1:5) on an ITO glass substrate at 3000 rpm for 30 s, and then annealed at 150 °C for 30 min. The cooled SnO$_2$ film was treated by UV-ozone for 45 min. Then, two-step solution method was used to deposit the perovskite film in an argon-filled glove box. The first step is to spin-coat the PbI$_2$ precursor solution (1.3 M PbI$_2$ and 3 wt% CsI in V_{DMF}:V_{DMSO}= 9:1) on the SnO$_2$ film (2500 rpm, 30 s) and heat it at 70 °C for 1 min. The second step is to spin-coat the mixed organic amine solution (0.12 M MAI, 0.05 M MABr, 0.03 M MACl and 0.23 M FAI are dissolved in IPA) on the PbI$_2$ film (2300 rpm, 30 s). And then, the samples are transferred to the air and annealed at 150 °C for 15 min to form a mixed perovskite film. Thenoyltrifluoroacetone (TTA) is dissolved in isopropanol

(IPA) to prepare different concentrations of TTA solutions (0.00 M, 0.20 M, 0.40 M, 0.60 M). After cooling to room temperature, the perovskite films were covered with TTA solution by spin-coating method (4000 rpm, 30 s) in the argon-filled glove box. Next, the solution used to prepare the hole transport layer (HTL) was prepared by dissolving 75.00 mg Spiro-OMeTAD, 35 μL Li-TFSI solution (260 mg mL^{-1} in acetonitrile), and 30 μL 4-tert-butylpyridine in 1 ml of chlorobenzene. And then, the HTL solution was spin-coated on the IL film in a glove box (3000 rpm, 30 s). The Ag with a thickness of 150 nm was prepared by the vacuum thermal evaporation method as the back contact electrode.

There is no change in device structure for humidity stability test, while the device structures for thermal stability test was changed. In the thermal stability test, FA$_{0.9}$Cs$_{0.1}$PbI$_3$ perovskite was used as the absorber due to the thermal instability of the MA containing perovskite. FA$_{0.9}$Cs$_{0.1}$PbI$_3$ perovskite was synthesized in two steps. The first step is to spin-coat the PbI$_2$ precursor solution (1.35 M PbI$_2$ and 10wt% CsI in V_{DMF}:V_{DMSO}= 9:1) on the SnO$_2$ film (2500 rpm, 30 s) and heat it at 70 °C for 1 min. The second step is to spin-coat the mixed organic amine solution (0.07 M FACl and 0.35 M FAI are dissolved in IPA) on the PbI$_2$ film (2000 rpm, 30 s). Furthermore, considering that Spiro-OMeTAD is an unstable HTL, we used mixed Spiro-OMeTAD/PTAA as HTL for thermal stability test. The mixed Spiro-OMeTAD/PTAA (36/5 mg mL^{-1}, dissolved in chlorobenzene) solution was employed with the addition of 35 μL Li-TFSI (260 mg mL^{-1}, dissolved in acetonitrile), and 30

µL 4-tertbutylpyridine, and deposited by spin-coating at 1500 rpm for 30s. At the same time, the gold was employed as the metal back electrode in thermal stability test.

1.3 Characterizations. The composition of the sample was verified by energy dispersive X-ray spectroscopy (EDS) and X-ray powder diffraction (BRUKER D8-ADVANCE). A field emission scanning electron microscope with a working voltage of 10 kV (FESEM, JEOL-JSM-6701F) was used to observe the characteristics of the cross section and the top surface. The ultraviolet-visible absorption spectrum of the sample were recorded with the Thermal Science Evolution 220 UV-Vis Spectrophotometer. The X-ray photoelectron spectroscopy (XPS) was used to study the interaction between TTA and perovskite lithium ion in Spiro-OMeTAD by the ESCAL-ab 220i-XL spectrometer (VG Scientific, England) with a monochromic Al Kα source at 1486.6 eV. Fourier transform infrared spectroscopy (FTIR) were recorded to characterize the interaction between TTA and perovskite and Li^+ by Tensor27, (BRUKER, Germany). The energy level of perovskite, TTA-modified perovskite, Spiro, and TTA-modified Spiro were measured with Ultraviolet Photoelectron Spectroscope (UPS, Thermo ESCALAB XI+) with a monochromatic He I light source (21.22 eV) and a VG Scienta analyzer. And the bias of -5 eV was applied to observe the secondary electron cut-off. Time-of-flight secondary ion mass spectrometry (TOF-SIMS) depth profiles was carried out to study the Li^+ migration behavior in devices. A dual-beam TOF-SIMS IV (IONTOF) spectrometer decorated with a 1 KeV, 1nA O^{2-} ion beam for the sputtering operated and a 30 keV, 1pA Bi_3^+ beam for the analysis in noninterlaced mode was used to test the degree of ion

migration. And the samples for TOF-SIMS characterization were aged in air for about 200 h. The Li, F, I, SnO and InO ions fragements act as the markers of Spiro-OMeTAD, TTA layer, perovskite film, SnO_2 layer and ITO respectively. Electrostatic potential (ESP) of TTA was calculated using density functional theory (B3LYP/3-21G). The confocal raman systems (iHR 550 HORIBA) with laser of 532 nm was utilized to characterize steady state photoluminescence (PL) spectra. The time-resolved fluorescence spectra (TRPL) were characterized by using a self-made inverted microscope (Nikon, TE2000-U) of the State Key Laboratory of Quantum Optics and Quantum Optical Devices of Shanxi University to scan a confocal system. The current density versus voltage ($J-V$) test and light intensity dependence curves were conducted using (CEL-AAAS50) assembled with a Keithley 2400 source meter. The light intensity was calibrated to AM 1.5G one sun (100 mW cm^{-2}) using a light irradiation meter and a standard Si photovoltaic cell. The J-V curves were measured from 0 V to 1.2 V (forward scan) or from 1.2 V to 0 V (reverse scan) with a scan rate of 100 mV s^{-1}. The size of the active area of the devices was defined to be 0.10 cm^2 by using a metal mask. The external quantum efficiency (EQE) was characterized by the Zennium CIMPS-pcs2 (Zahner) system assembled with the tunable light source (TLS03). The space-charge-limited current (SCLC) and dark J-V characteristics of devices were measured using a Keithley 2400 source meter in applied voltage from 0.0 V to 2.5 V and -1.0 V to 1 V, repectively. Mott-Schottky plots was measured with a impedance potential method of CHI660E workstation under dark conditions. I-V characteristic in the voltage range of -1.2 V to 1.2V and electrochemical impedance

spectroscopy (EIS) with a bias of 0.8 V in the frequency range of 1 MHz to 1 Hz was conducted to study the carrier recombination dynamics by CHI660E workstation. The un-encapsulated devices for stability measurement were aged at 25 °C in different aging conditions, including in dark moisture-proof box with the humidity of 1%-2% RH , in dark air condition with the humidity of 10%-20% RH, and in air condition with the humidity of 50%-60% RH, and heating at 60°C in a dark argon-filled glove box. And the values presented in stability measurement are the average values of at least 20 devices.

1.4 Computational Details and Models. All density functional theory (DFT) calculations were performed using the Vienna *ab initio* Simulation Package (VASP).[S1-S2] The augmented plane wave (PAW) method was used to describe the electron–ion interactions.[S3] The generalized gradient approximation (GGA) with the Perdew-Burke-Ernzerhof parameterization (PBE) was applied to handle the exchange and correlation functionals.[S4] The plane wave cut-off energy was set to be 400 eV. The Gaussian smearing method[S5] with 0.1 eV width was employed to determine the electron occupancy. The k-point interval distribution of Monkhorst-Pack[S6] was 0.2 Å^{-1} for structural optimization. Vacuum space of 20 Å was employed in the z direction to avoid any spurious interaction. Spurious dipole interactions between periodic images were corrected by the dipole correction (IDIPOL=3). To consider the van der Waals interaction, the long-range dispersion forces are accounted for using the Grimme DFT-D3 method[S7,S8].The crystal structures, charge density difference isosurfaces, and contour plots were generated by the VESTA program.[S9] The

migration barriers of ions were studied by the standard nudged elastic band (NEB) method,[S10] which has been well demonstrated to identify the right transition state (TS) structure.[S11]
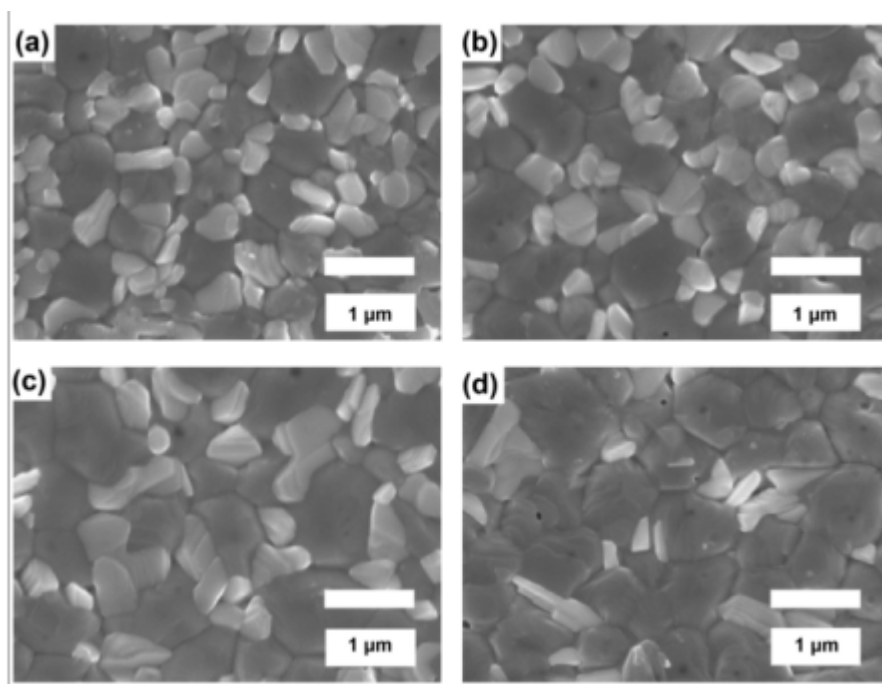

Fig. S1. Top-view SEM images of the perovskite films with different concentration of TTA modification: (a) 0.0 M, (b) 0.2 M, (c) 0.4 M, and (d) 0.6 M, respectively.
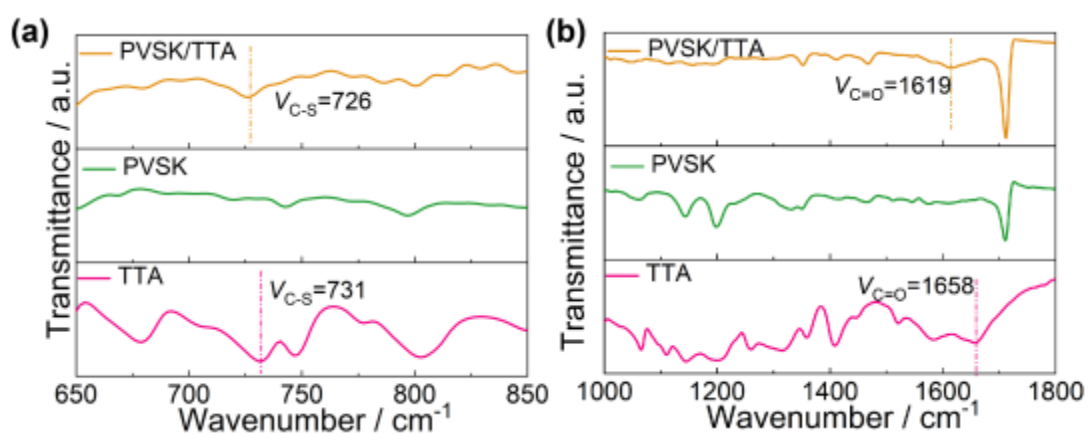

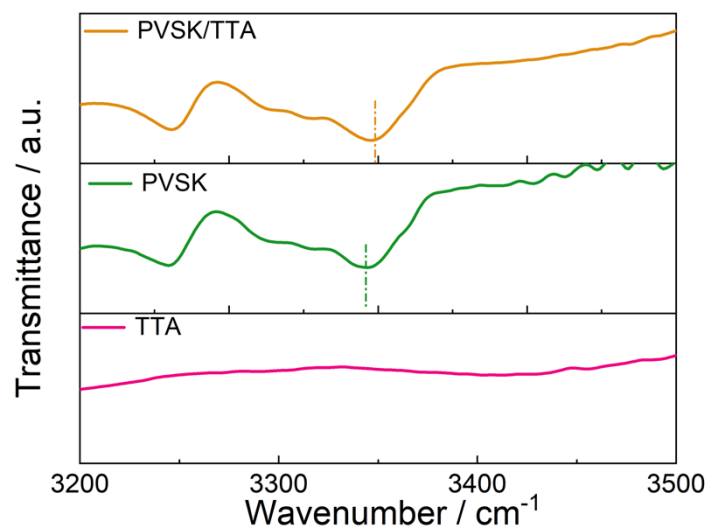**Fig. S2.** FTIR spectra of TTA, PVSK and PVSK/TTA at different wavenumber ranges: (a) 650-800 cm^{-1}; (b)1000-1800 cm^{-1}.

Fig. S3. FTIR spectra of TTA, PVSK and PVSK/TTA at 3200-3500 cm^{-1} range.
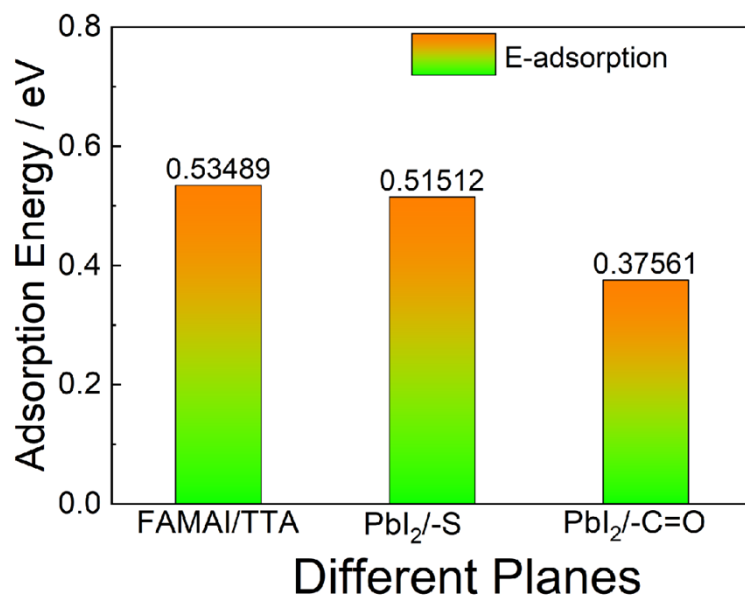
Fig. S4. The adsorption energy of TTA on PbI_2 plane and FAMAI plane of perovskite with different adsorption sites.
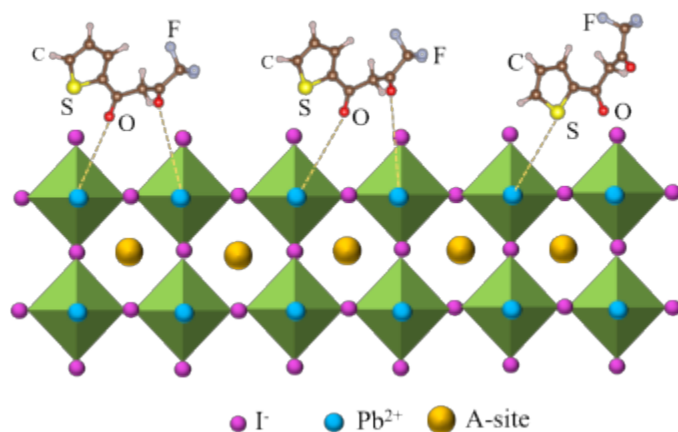
Fig. S5. Structure diagram of TTA passivated perovskite interface
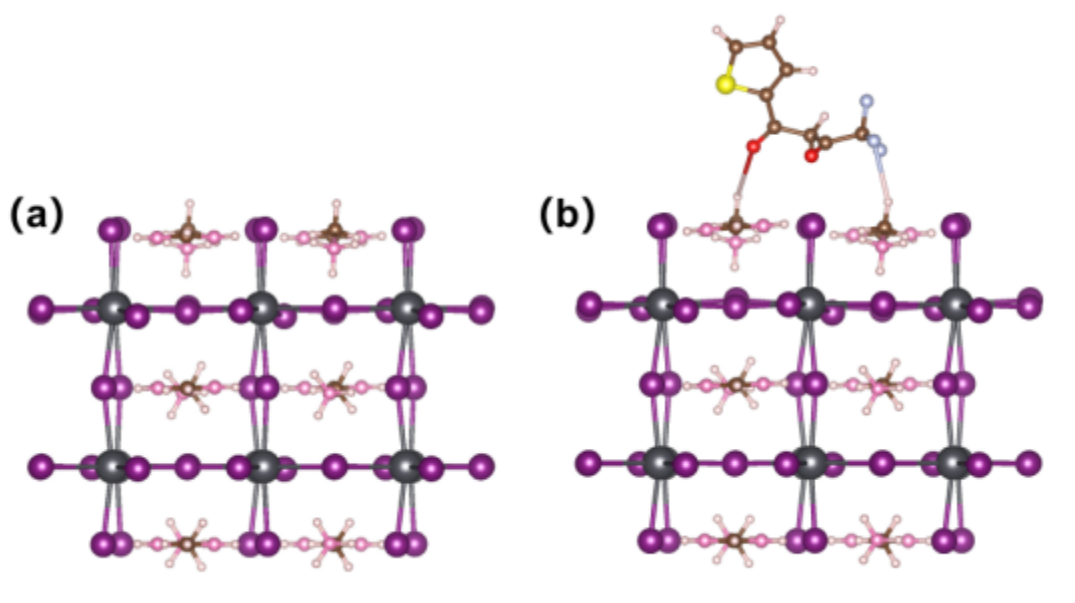

Fig. S6. (a) Simulated model of organic FAMAI slab in perovskite, (b) simulated interaction model of TTA molecule and FAMAI slab with -C=O and F sites.
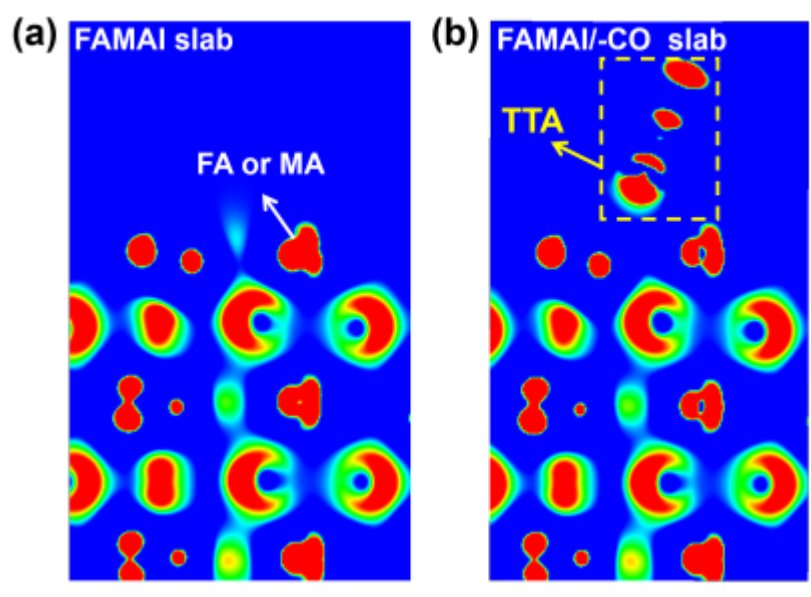
Fig. S7. 2D visual charge density difference of (100) plane section with isovalue of 0.002 e Å^{-3} for FAMAI-terminal perovskite film (a) W/O and (b) with TTA modification using -C=O site.
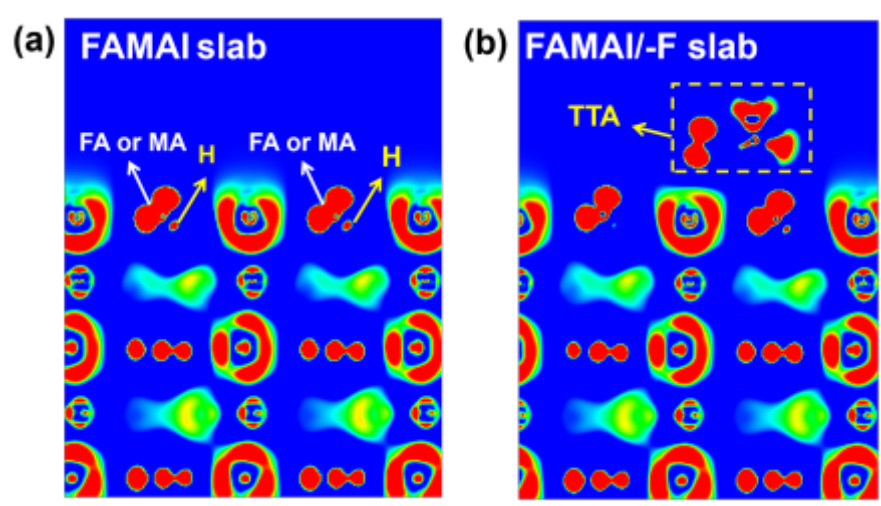

Fig. S8. 2D visual charge density difference of (110) plane section with isovalue of 0.002 e Å^{-3} for FAMAI-terminal perovskite film (a) W/O and (b) with TTA modification using -F site.
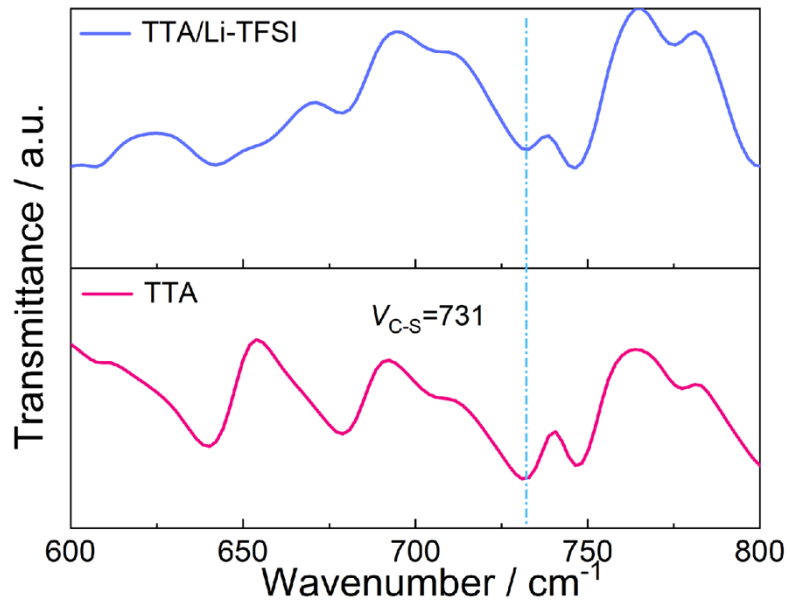
Fig. S9. FTIR spectra of TTA and TTA/Li-TFSI at 600-800 cm^{-1} range.
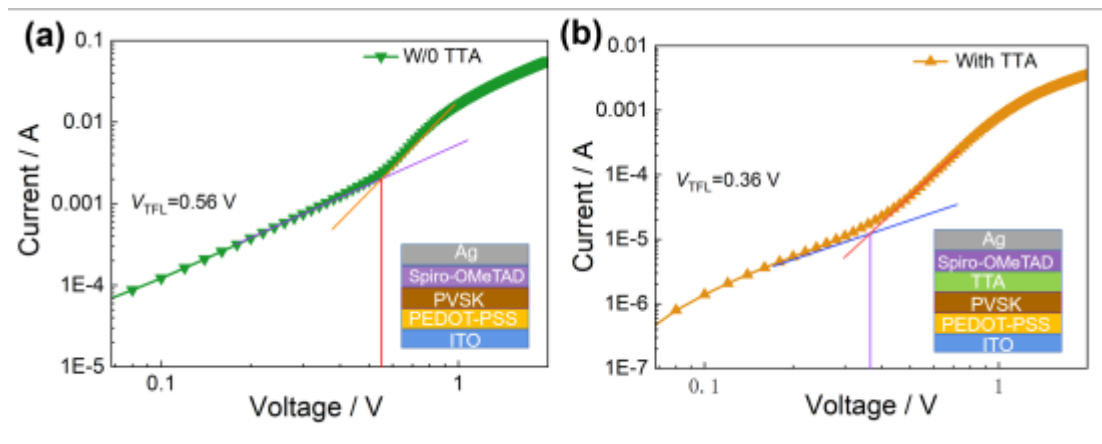
\

Fig. S10. The carrier space-charge-limied current (SCLC) curves of devices: (a) W/O TTA and (b) With TTA.
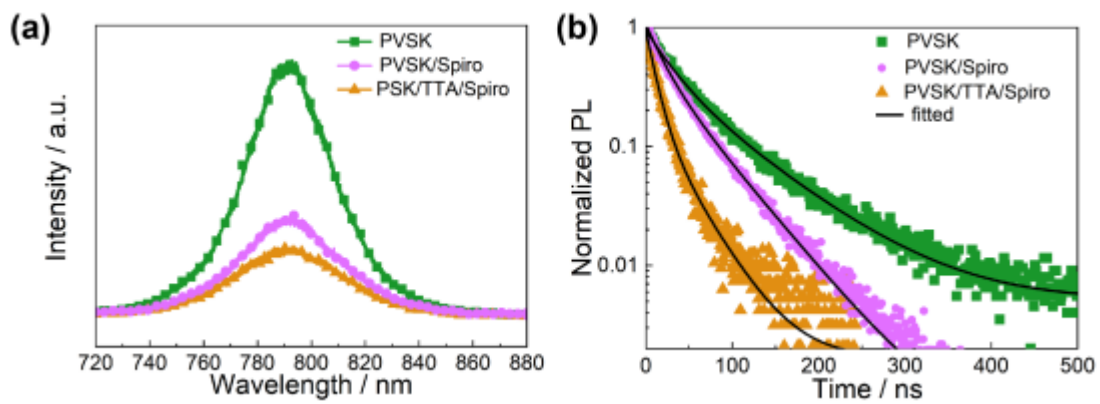
Fig. S11. (a) PL and (b) TRPL spectra for PVSK, PVSK/Spiro and PVSK/TTA/Spiro based on the glass substrate, respectively.
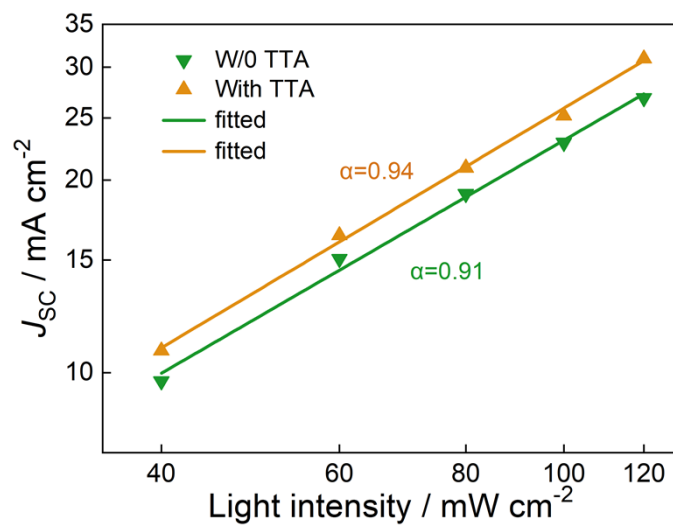

Fig. S12. Light intensity dependent J_{SC} curves of devices W/O or with TTA modification.
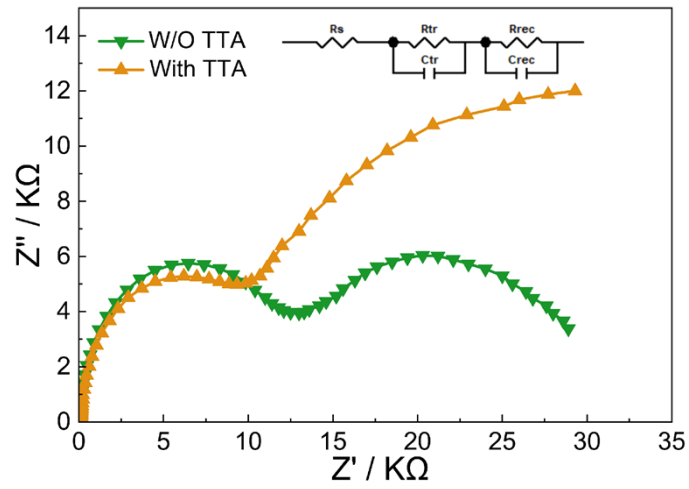
Fig. S13. Nyquist plots of the PSCs W/O TTA and with TTA measured at a bias of 0.8 V in the frequency range of 1 MHz to 1 Hz under dark condition.

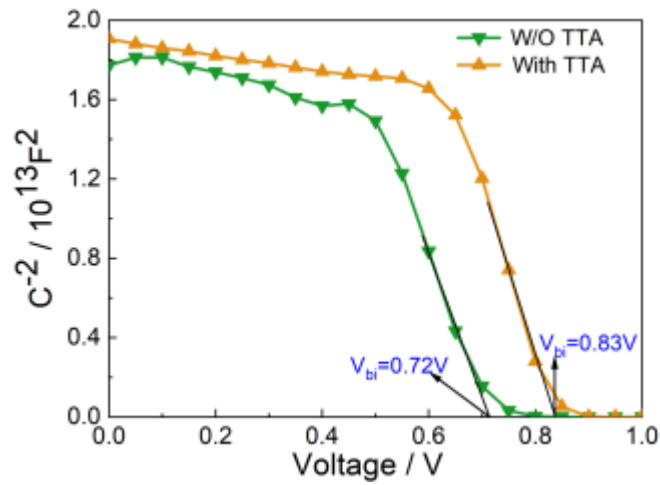
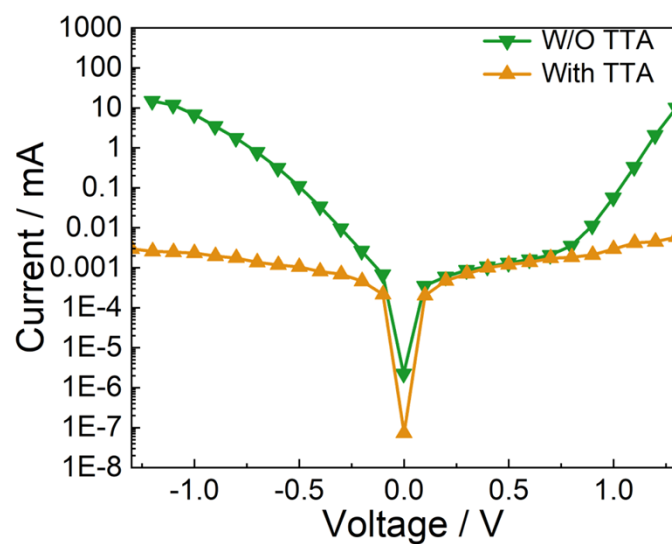**Fig. S14.** Mott-Schottky plots of devices W/O or with TTA modification.

Fig. S15. Dark *J-V* characteristics of devices W/O or with TTA modification.
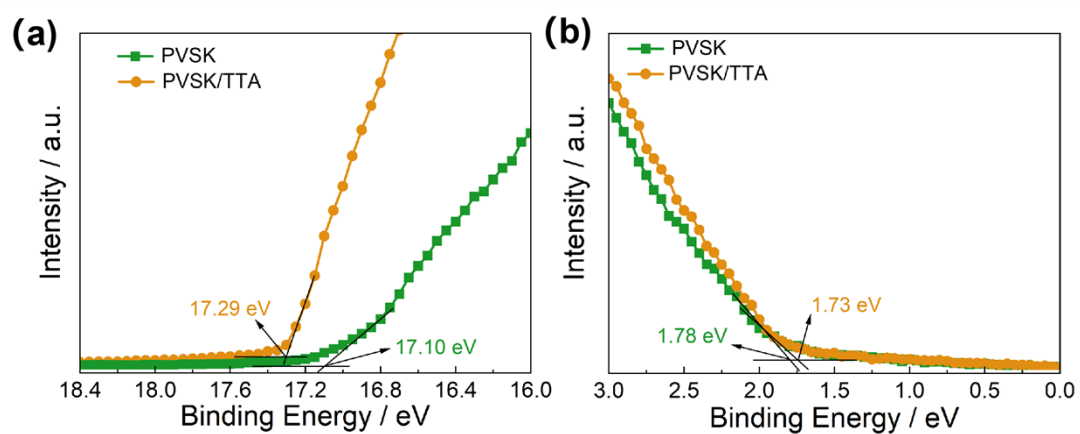
Fig. S16. (a) Cutoff and (b) onset region of PVSK and PVSK/TTA.
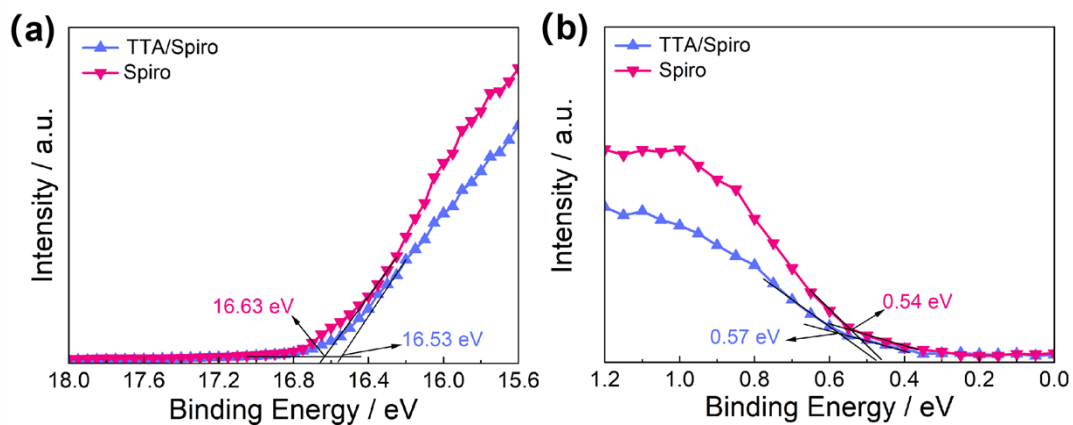
Fig. S17. (a) Cut-off and (b) onset region of Spiro-OMeTAD and TTA/Spiro-OMeTAD.
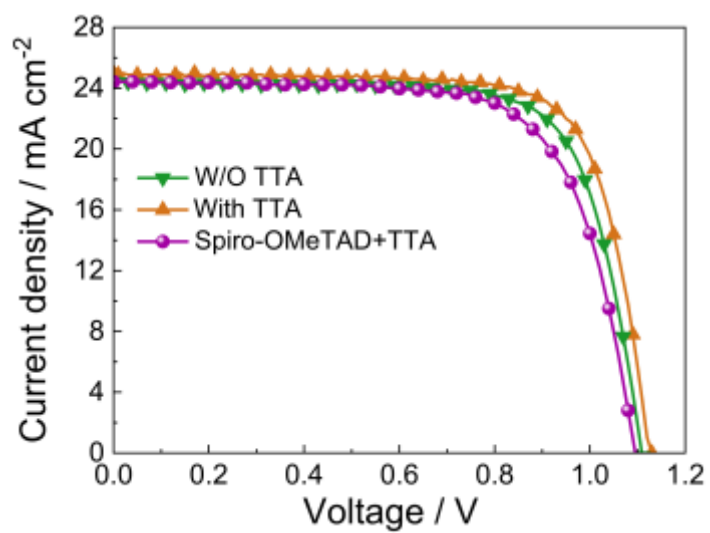
Fig.S18 Reverse scanned *J-V* curves
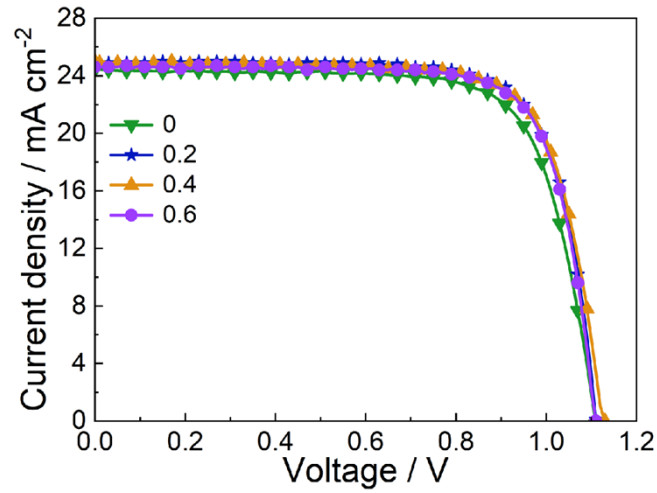
Fig. S19. Reverse scanned *J-V* curves based TTA modification with different concentraton.
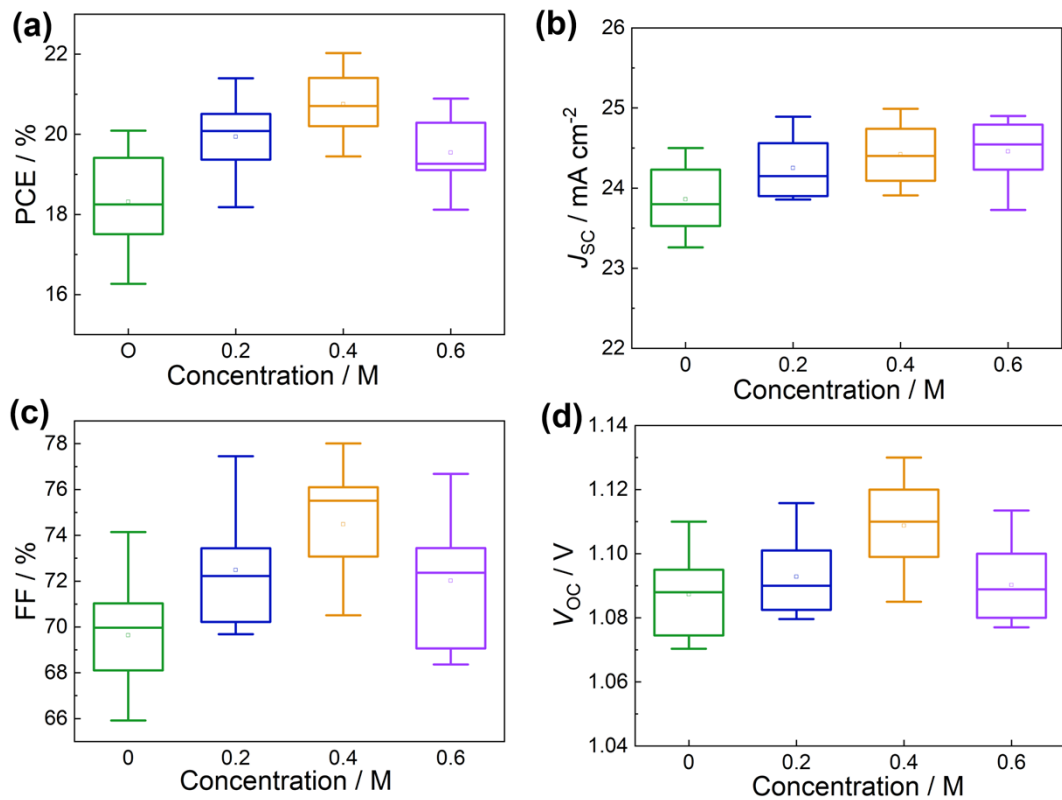
Fig. S20. The statistical analysis results of performance parameters based on 20 devices: (a) Power conversion effiency (PCE) distribution; (b)Short current density (J_{SC}) distribution ; (c) Fill factor (FF) distribution ; (d) Open circuit voltage (V_{OC}) distribution.
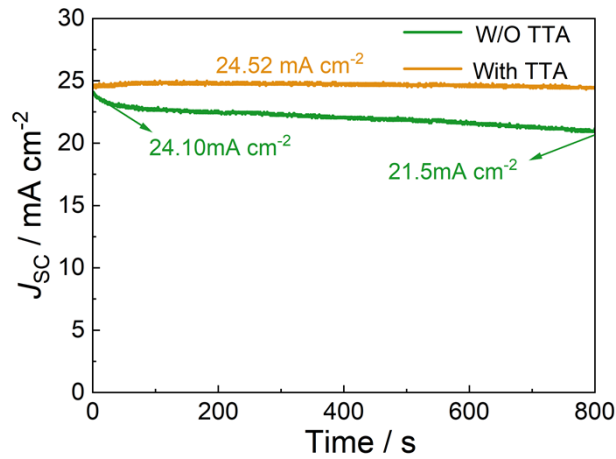
Fig. S21. Steady-state J_{SC} versus time for the best-performing devices W/O and with TTA at the maximum power point.
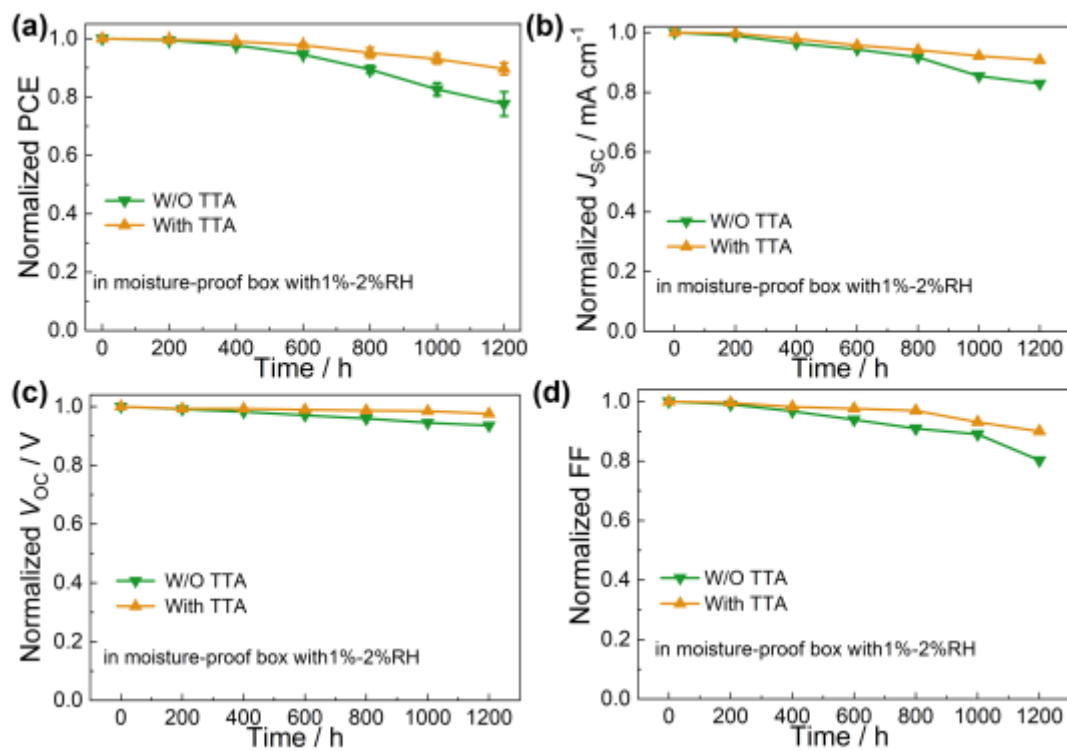
Fig. S22. Normalized performance parameters evolution of unencapsulated devices W/O and with TTA modification aged at dark conditions in moisture-proof box with the humidity of 1%-2% RH: (a) PCE; (b) J_{SC}; (c) V_{OC} and (d) FF.
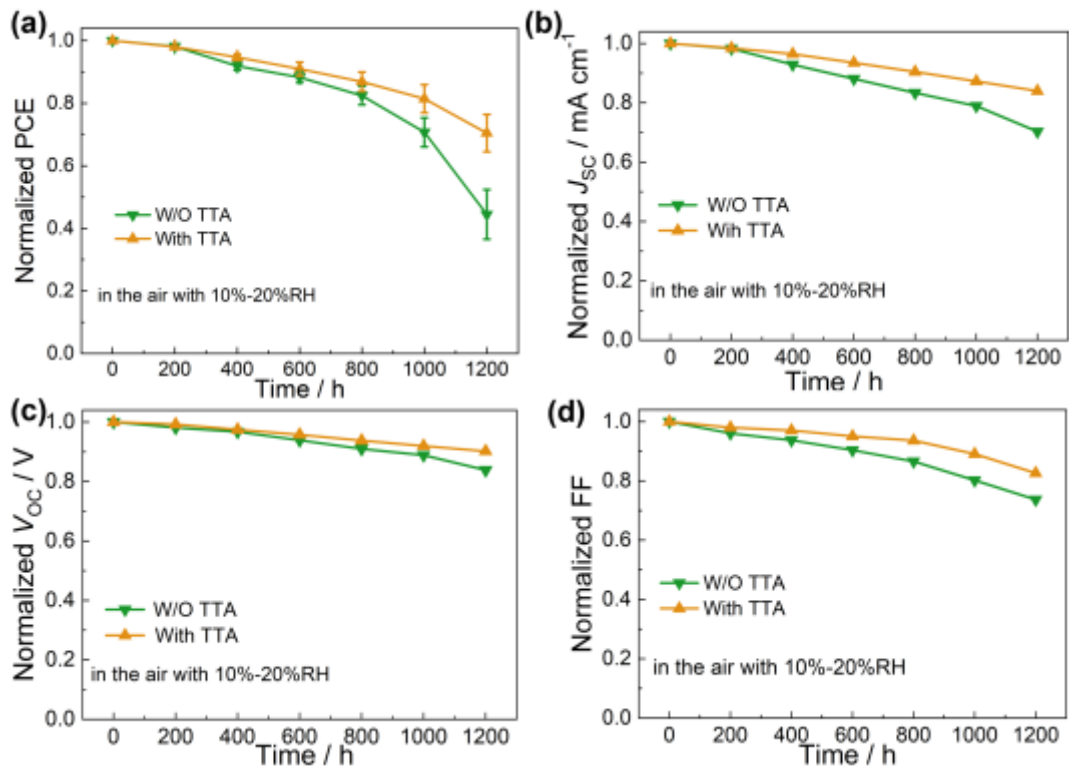
Fig. S23. Normalized performance parameters evolution of unencapsulated devices W/O and with TTA modification aged at dark conditions in air condition with the humidity of 10%-20% RH: (a) PCE; (b) J_{SC}; (c) V_{OC} and (d) FF.
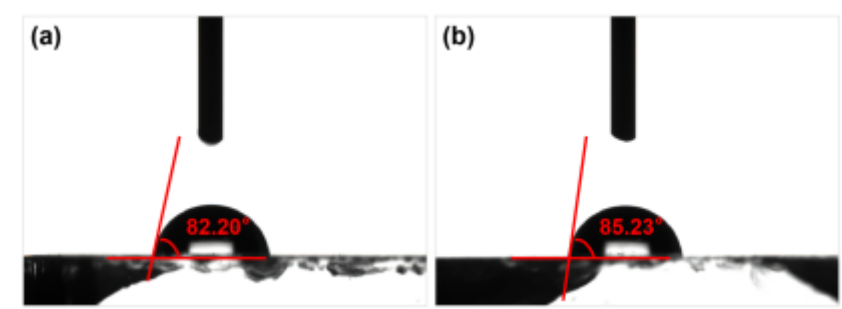
Fig. S24. The contact angle of perovskite film: (a) W/O and (b) with TTA modification.
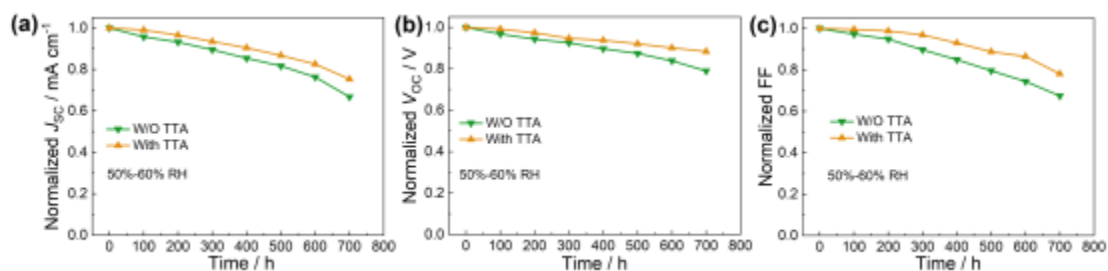
Fig. S25. Normalized performance parameters evolution of unencapsulated devices W/O and with TTA modification aged at 60°C in a dark argon-filled glove box: (a) J_{SC}; (b) V_{OC} and (c) FF.
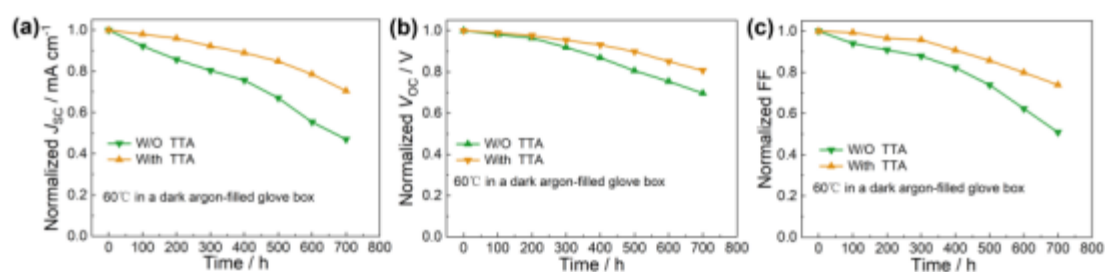
Fig. S26. Normalized performance parameters evolution of unencapsulated devices W/O and with TTA modification aged at 60°C in a dark argon-filled glove box: (a) J_{SC}; (b) V_{OC} and (c) FF.

Table S1. Li^+ migrate energy of three states in film W/O and with TTA.

Li^+ migrate states	initial	transition	final
W/O TTA	-473.19	-472.82	-472.97
With TTA	-594.72	-594.05	-594.23

Table S2. TRPL data with and W/O TTA modification.

Samples	A_1	τ_1 (ns)	A_2	τ_2 (ns)	τ_{ave} (ns)
PVSK	0.44	78.62	0.56	27.14	62.90
PVSK/TTA	0.54	48.71	0.46	144.88	117.66
PVSK/Spiro	0.51	18.08	0.49	50.09	41.34
PVSK/TTA/Spiro	0.81	10.46	0.19	35.40	21.70

Table S3. Champion and average photovoltaic performances parameters of PSCs with and W/O TTA modification.

Samples		V_{OC} (V)	J_{SC} (mA cm^{-2})	FF (%)	PCE (%)
W/O TTA	average	1.09±0.02	23.85±0.65	70.17±3.99	18.25±1.84
	champion	1.11	24.50	74.15	20.17
With TTA	average	1.11±0.02	24.49±0.50	74.67±2.88	20.67±1.22
	champion	1.13	24.99	78.01	22.03

Table S4. Summary of photovoltaic performance of reported high-efficiency Cs-MA-FA-based PSCs in recent years.

Device structure	J_{SC} (mA/cm^2)	V_{OC} (V)	FF	PCE (%)	Active area (cm^2)	Ref.
ITO/SnO$_2$/(Cs$_{0.05}$FA$_{0.54}$MA$_{0.41}$)Pb(I$_{0.98}$Br$_{0.02}$)$_3$/TTA/Spiro-OMeTAD/Ag	**24.99**	**1.13**	**0.78**	**22.03**	**0.1**	**This work**
ITO/SnO$_2$/FA$_{0.80}$MA$_{0.15}$Cs$_{0.05}$PbI$_{2.55}$Br$_{0.4}$/HABr/Spiro-OMeTAD/Au	23.70	1.23	0.81	23.60	0.0706	S12
FTO/TiO$_2$/(Cs$_{0.05}$(MA$_{0.17}$FA$_{0.83}$)$_{0.95}$Pb(I$_{0.83}$Br$_{0.17}$)$_3$)/Spiro-OMeTAD/Au	22.96	1.13	0.76	19.69	0.1	S13
FTO/TiO$_2$/Rb$_{0.05}$Cs$_{0.05}$FA$_{0.8}$MA$_{0.07}$PbI$_{2.57}$Br$_{0.4}$/LiTFSI-Free Spiro-OMeTAD/Au	22.70	1.10	0.73	18.3	1	S14
ITO/(SnO$_2$-PEIE)/(PCBM/MnSO$_4$)/MA$_{0.10}$Cs$_{0.05}$FA$_{0.85}$Pb(I$_{0.95}$Br$_{0.05}$)$_3$/PDCB/PTAA-BCF/Au	24.20	1.11	0.78	20.90	0.113	S15
FTO/TiO$_2$/SnO$_2$/(PbI$_2$:PbBr$_2$:FAI:MAI:CsI:MACl=0.98:0.02:0.81:0.04:0.05:0.20)/PDEAI$_2$/Spiro-OMeTAD)/Au	24.75	1.16	0.83	23.92	0.09	S16
FTO/SnO$_2$/Cs$_{0.05}$(MA$_{0.17}$FA$_{0.83}$)$_{0.95}$Pb(I$_{0.83}$Br$_{0.17}$)$_3$/Spiro-OMeTAD/Au	23.05	1.13	0.80	20.79	0.09	S17
FTO/SnO$_2$/Cs$_{0.05}$(MA$_{0.17}$FA$_{0.83}$)$_{0.95}$Pb(I$_{0.83}$Br$_{0.17}$)$_3$/Spiro-OMeTAD/Au	22.75	1.16	0.74	19.51	0.08	S18
FTO/TiOxNy/meso-TiO$_2$/PMMA:PCBM/Cs$_{0.05}$FA$_{0.9}$MA$_{0.05}$PbI$_{2.74}$Br$_{0.26}$/PMMA/P$_3$HT:CuPc/Au	22.80	1.19	0.86	23.36	1	S19
FTO/TiO$_2$/Cs$_{0.05}$(FA$_{0.83}$MA$_{0.17}$)$_{0.95}$Pb(I$_{0.83}$Br$_{0.17}$)$_3$/C-Spiro-OMeTAD	24.77	1.15	0.82	23.56	0.125	S20
FTO/SnO$_2$/Cs$_{0.05}$(MA$_{0.13}$FA$_{0.87}$)$_{0.95}$Pb(I$_{0.87}$Br$_{0.13}$)$_3$/Zn(C$_6$F$_5$)$_2$-P3HT/Au	24.81	1.02	0.69	17.49	No	S21
ITO/SnO$_2$/Cs$_{0.05}$(FA$_{0.85}$MA$_{0.15}$)$_{0.95}$Pb(I$_{0.85}$Br$_{0.15}$)$_3$/Sb$_2$S$_3$-Spiro-OMeTAD/Au	24.75	1.13	0.79	22.13	0.04	S22

Table S5. Reverse and forward scan photovoltaic parameters of PSCs with and W/O TTA modification.

Samples	Scan directions	V_{OC} (V)	J_{SC} (mA cm^{-2})	FF (%)	PCE (%)	HI
W/O TTA	RS	1.11	24.50	74.15	20.17	0.05
	FS	1.10	24.20	72.04	19.18	
With	RS	1.13	24.99	78.01	22.03	0.03
TTA	FS	1.12	24.90	76.37	21.30	

Table S6. Photovoltaic performances parameters of PSCs based on modified by TTA with different concentration.

Samples		V_{OC} (V)	J_{SC} (mA cm^{-2})	FF (%)	PCE (%)
0	average	1.090±0.02	23.85±0.65	70.17±3.99	18.25±1.84
	champion	1.110	24.50	74.15	20.17
0.2	average	1.091±0.02	24.26±0.63	74.26±3.19	19.88±1.52
	champion	1.111	24.89	77.45	21.41
0.4	average	1.111±0.02	24.49±0.50	74.67±2.88	20.67±1.22
	champion	1.130	24.99	78.01	22.03
0.6	average	1.092±0.02	24.30±0.60	73.01±3.67	19.26±1.63
	champion	1.113	24.59	76.68	20.98

References:

S1 G. Kresse and J. Furthmüller, Efficiency of ab-initio total energy calculations for metals and semiconductors using a plane-wave basis set, *Comput. Mater. Sci.,* 1996, **6**, 15–50.

S2 G. Kresse and D. Joubert, From ultrasoft pseudopotentials to the projector augmented-wave method, *Phys. Rev. B,* 1999, **59**, 1758–1775.

S3 P. E. Blöchl, Projector augmented-wave method, *Phys. Rev. B,* 1994, **50**, 17953–17979.

S4 J. P. Perdew, K. Burke and M. Ernzerhof, *Phys. Rev. Lett.,* 1996, **77**, 3865–3868.

S5 M. Methfessel and A. T. Paxton, Generalized Gradient Approximation Made Simple, *Phys. Rev. B,* 1989, **40**, 3616–3621.

S6 J. D. Pack and H. J. Monkhorst, "Special points for Brillouin-zone integrations"—a reply, *Phys. Rev. B,* 1977, **16**, 1748–1749.

S7 S. Grimme, Semiempirical GGA-type density functional constructed with a long-range dispersion correction, *J. Comput. Chem.,* 2006, **27**, 1787–1799.

S8 S. Küfner, A. Schleife, B. Höfflfling and F. Bechstedt, Energetics and approximate quasiparticle electronic structure of low-index surfaces of SnO_2, *Phys. Rev. B,* 2012, **86**, 075320.

S9 K. Momma and F. Izumi, VESTA: a three-dimensional visualization system for electronic and structural analysis, *J. Appl. Crystallogr.,* 2008, **41**, 653–658.

S10 N. Govind, M. Petersen, G. Fitzgerald, D. King-Smith and J. Andzelm, A generalized synchronous transit method for transition state location, *Comput.*

Mater. Sci., 2003, **28**, 250.

S11 P. Xiang, X. F. Chen, J. Liu, B. B. Xiao and L. Y. Yang, Borophene as Conductive Additive to Boost the Performance of MoS$_2$-Based Anode Materials, *J. Phys. Chem. C,* 2018, **122**, 9302–9311.

S12 S. Tang, J. Bing, J. Zheng, J. Tang, Y. Li, M. Mayyas, Y. Cho, T. Jones, T. Yang, L. Yuan, M. Tebyetekerwa, H. Nguyen, M. Nielsen, N. Ekins-Daukes, K. Kalantar-Zadeh, G. Wilson, D. McKenzie, S. Huang and A. Ho-Baillie, Complementary bulk and surface passivations for highly efficient perovskite solar cells by gas quenching, Cell Rep.Phys. Sci., 2021, 2, 100511.

S13 P. Q.Yuan, J. H. Wu, W. H. Sun, Q. J. Zhu, M. J. Zhang, J. J. Zou, X. B. Wang, X. P. Liu, Y. Q.Yang, and Z. Lan, High-Performance Perovskite Solar Cells Using Iodine as Effective Dopant for Spiro-OMeTAD, Energy Technol., 2020, 8, 1901.

S14 B. Tan, S. R. Raga, A. S. R. Chesman, S. O. Fürer, F. Zheng, D. P. McMeekin, L. C. Jiang, W. X. Mao, X. F. Lin, X. M. Wen, J. F. Lu, Y. B. Cheng, and U. Bach, LiTFSI-Free Spiro-OMeTAD-Based Perovskite Solar Cells with Power Conversion Efficiencies Exceeding 19%, Adv. Energy Mater., 2019, 9, 19015.

S15 Y. Zhao, T. Heumueller, J. Zhang, J. Luo, O. Kasian, S. Langner, C. Kupfer, B. Liu, Y. Zhong, J. Elia, A. Osvet, J. Wu, C. Liu, Z. Wan, C. Jia, N. Li, J. Hauch and C. Brabec, A bilayer conducting polymer structure for planar perovskite solar cells with over 1,400 hours operational stability at elevated temperatures, Nat. Energy, 2022, 7, 144-152.

S16 C. Liu, Y. Yang, K. Rakstys, A. Mahata, M. Franckevicius, E. Mosconi, R. Skackauskaite, B. Ding, K. Brooks, O. Usiobo, J. Audinot, H. Kanda, S. Driukas, G. Kavaliauskaite, V. Gulbinas, M. Dessimoz, V.utas Getautis, F. Angelis, Y. Ding, S. Dai, P. Dyson and M. Nazeeruddin, Tuning structural isomers of phenylenediammonium to afford efficient and stable perovskite solar cells and modules, Nat. Commun., 2021, 12, 6394

S17 G. Yang, C. Chen, F. Yao, Z. Chen, Q. Zhang, X. Zheng, J. Ma, H. Lei, P. Qin, L.Xiong, W. Ke, G. Li, Y. Yan and G. Fang, Effective Carrier-Concentration Tuning of SnO2 Quantum Dot Electron-Selective Layers for High-Performance Planar Perovskite Solar Cells, Adv. Mater., 2018, 30, 1706023.

S18 J. Ma, X. Zheng, H. Lei, W. Ke, C. Chen, Z. Chen, G. Yang and G. Fang, Highly Efficient and Stable Planar Perovskite Solar Cells With Large-Scale Manufacture of E-Beam Evaporated SnO2 Toward Commercialization, Sol.RRL, 2017, 1, 1700118.

S19 J.Peng, F. Kremer, D. Walter, Y. Wu, Y. Ji, J. Xiang, W. Liu, T. Duong, H. Shen, T. Lu, F. Brink, D. Zhong, L. Li, O. Lee, C. Lem, Y. Liu, K. Weber, T. White and K. Catchpole, Centimetre-scale perovskite solar cells with fill factors of more than 86 percent, Nature, 2022, 601, 573-578.

S20 S. B. Wang , F. X. Cao, P. X. Chen, R. W. He, A. L. Tong, Z. Lan, P. Gao, W. H. Sun, and J. H. Wu, Two birds with one stone: Simultaneous realization of constructed 3D/2D heterojunction and p-doping of hole transport layer for highly efficient and stable perovskite solar cells, Chem.Eng.J., 2023, 453, 139721.

S21 Q. K. Hu, E. Rezaee, M. Z. Li, Q. Chen, C. Li, S. Y. Cai, H. Q. Shan, and Z. X. Xu, P3HT with $Zn(C_6F_5)_2$ as p-Type Dopant for the Enhanced Performance of Planar Perovskite Solar Cells, Sol. RRL, 2020, 4, 1900340.

S22 Q. Du, Z. T. Shen, C. Chen, F. M. Li, M. Q. Jin, H. L. Li, C. Dong, J. H. Zheng, M. X. Ji, and M. T. Wang, Spiro-OMeTAD:Sb_2S_3 Hole Transport Layer with Triple Functions of Overcoming Lithium Salt Aggregation, LongTerm High Conductivity, and Defect Passivation for Perovskite Solar Cells, Sol. RRL, 2021, 5, 2100622.